Chemical alteration of fine-grained sedimentary rocks at Gale crater

N. Mangold, E. Dehouck, C Fedo, O. Forni, C Achilles, T. Bristow, R T Downs, J. Frydenvang, O. Gasnault, J L'Haridon, et al.

Chemical alteration of fine-grained sedimentary rocks at Gale crater

N. Mangold[1*], E. Dehouck[2], C. Fedo[3], O. Forni[4], C. Achilles[5], T. Bristow[6], R. T. Downs[5], J. Frydenvang[7], O. Gasnault[4], J. L'Haridon[1], L. Le Deit[1], S. Maurice[4], S.M. McLennan[8], P.-Y. Meslin[4], S. Morrison[5], H.E. Newsom[9], E. Rampe[10], W. Rapin[11], F. Rivera-Hernandez[12], M. Salvatore[13], R.C. Wiens[14].

[1]Laboratoire de Planétologie et Géodynamique, CNRS, UMR 6112, Université de Nantes, Université d'Angers, Nantes, France, nicolas.mangold@univ-nantes.fr. [2]Laboratoire de Géologie de Lyon, Université Claude Bernard, CNRS, France, [3]Dept Earth Planetary Sci., University of Tennessee, Knoxville, USA, [4]IRAP, UPS-OMP, Université de Toulouse, Toulouse, France, [5]Department of Geosciences, University of Arizona, Tucson, USA, [6]NASA Ames Research Center, Moffett Field, USA, [7]Natural History Museum of Denmark, University of Copenhagen, Denmark [8]Stony Brook Univ, Stony Brook, New York, USA, USA, [9]U. New Mexico, Albuquerque, NM 87131, USA, [10]Aerodyne Industries, JETS at NASA JSC, Houston, [12]UC Davis Earth and Planetary Science, Davis, California,[11]Caltech/JPL, Pasadena, USA, [13]Dept Physics Astronomy, NAU, Flagstaff, USA, [14]Los Alamos National Laboratory, Los Alamos, New Mexico, USA.

*Corresponding author

Abstract

From Sol 750 to 1550, the Curiosity rover documented >100 m thick stack of fine-grained sedimentary rocks making up part of the Murray formation, at the base of Mt Sharp, Gale crater. Here, we use data collected by the ChemCam instrument to estimate the level of chemical weathering in these sedimentary rocks. Both the Chemical Index of Alteration (CIA) and the Weathering Index Scale (WIS) indicate a progressive increase in alteration up section, reaching values of CIA of 63 and WIS of 25%. The increase in CIA and WIS values is coupled with a decrease in calcium abundance, suggesting partial dissolution of Ca-bearing minerals (clinopyroxene and plagioclase). Mineralogy from the CheMin X-ray diffraction instrument indicates a decrease in mafic minerals compared with previously analyzed strata and a significant proportion of phyllosilicates consistent with this interpretation. These observations suggest that the sediments were predominantly altered in an open system, before or during their emplacement, contrasting with the rock-dominated conditions inferred in sedimentary deposits analyzed at Yellowknife Bay.

1. Introduction

Gale crater was formed in the ancient crust of Mars close to the topographic dichotomy boundary ca. 3.6-3.7 Ga, i.e. near the Late Noachian-Early Hesperian boundary (Anderson and Bell, 2010, Le Deit et al., 2013). The site was selected as a landing site for the Mars Science Laboratory (MSL) Curiosity rover for its ~5 km-high central mound composed of sedimentary deposits, where clay and sulfate mineral signatures were detected by orbital spectrometry in the lower units (Milliken et al., 2010). Although the Curiosity rover has not yet accessed the orbitally-detected clay minerals, previous analyses from the CheMin X-Ray diffractometer (XRD) showed that clay minerals were present in the lacustrine mudstones at Yellowknife Bay (Vaniman et al., 2014, Bristow et al., 2015). These rocks are part of a succession which also includes fluvial sandstones and conglomerates (Grotzinger et al., 2014). After 750 Sols (martian days) and 9-km of traverse, clay minerals were detected again by CheMin in the sedimentary rocks of the Murray formation, the basal unit of the Mt Sharp group, informally named the Pahrump Hills member (Rampe et al., 2017, Bristow et al., 2017).

At Pahrump Hills, variations in chemistry and mineralogy over a ~10-meter high sequence indicated transitions from hematite-dominated to magnetite-dominated mineralogical assemblages interpreted as due either to diagenetic episodes from multiple influxes of groundwater (Rampe et al., 2017) or variations in pH and Eh of the lake waters (Hurowitz et al., 2017). From Sol 750 to Sol 1550, the rover traversed six more km of various terrains, dominated by the Murray formation totaling ~130 m of stratigraphy, enabling a more in-depth assessment of this sedimentary unit (Fig. 1).

Our study focuses on the chemical indices of alteration through the whole column of Murray sedimentary rocks in the studied sol range (750-1550). Data collected by the ChemCam instrument suite are used to assess the chemistry of Murray rocks. The ChemCam Laser Induced Breakdown Spectrometer (LIBS) provides elemental analyses of rocks and soils from their ablation by a pulsed laser, and the Remote Micro-Imager (RMI) provides images for context and textural analysis (Wiens et al., 2012, Maurice et al., 2012). CheMin X-ray diffraction data (Blake et al., 2012) are used to assess locally the mineralogy of the Murray formation in order to better understand the type of aqueous alteration observed on these sedimentary rocks. Results of both instruments are consistent, showing that significant aqueous alteration took place at Gale crater. We discuss further the origin and significance of this alteration.

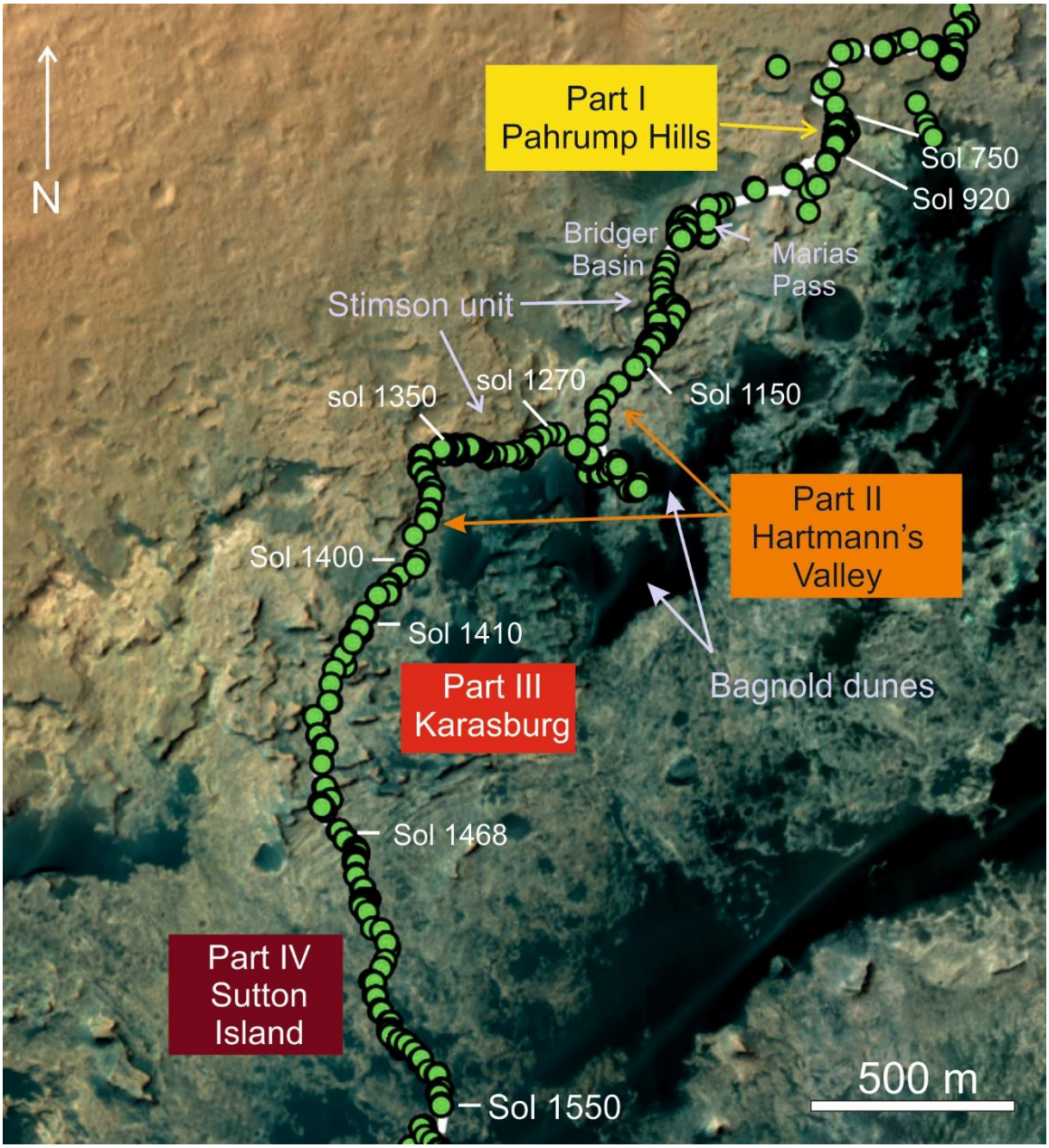

Fig. 1: (a) Context orbital image of the Curiosity traverse from the Bradbury Landing Site to sol 1600. (b) High Resolution Imaging Science Experiment (HiRISE) color image of Gale crater along the traverse of the rover showing the areas of Murray formation outcrops analyzed in this study. The Murray formation was divided in four members: (1) Pahrump Hills (sols 750-920); (2) Hartmann's Valley (sols 1170-1250 and sols 1350-1400); (3) Karasburg (sols 1410-1467); (4) Sutton Island (sols 1468-1550). Green disks indicate locations of ChemCam analyses along the rover traverse.

2. Dataset

2.1 Chemcam data

The ChemCam instrument suite consists of a LIBS coupled with the RMI which provides images for context and textural analysis (Wiens et al., 2012, Maurice et al., 2012). The LIBS technique uses a pulsed laser to ablate the rocks, producing a plasma. The atomic emission spectrum of the plasma is analyzed by three spectrometers in the spectral ranges of the ultra-violet (240–342 nm), visible violet (382–469 nm), and visible/near-infrared (474–906 nm). By using ChemCam LIBS spectra, the emission lines of all major elements (Si, Al, K, Na, Ca, Mg, Fe, Ti), as well as several minor and trace elements (Li, Mn, Cr, Zn, Ni, Sr, Rb, Ba, Cu) can be identified (e.g., Ollila et al., 2014). Volatiles and halogens (O, S, P, H, Cl, F) can also be identified if present in sufficient proportions (i.e., >1-10% depending on elements, Meslin et al., 2013, Forni et al., 2015). Carbon is detected in all targets analyzed and corresponds to the contribution of atmospheric carbon dioxide (Meslin et al., 2013).

Quantification of major elements is achieved by multivariate analyses using a range of emission lines and comparing them to 450 standards analyzed in a testbed (Clegg et al., 2017). The ChemCam laser beam focuses to a small spot, typically ~350-550 μm in diameter (medium sand in size) at distances of 2–5 m. LIBS data are usually collected in lines of 5 to 20 points or matrices of 3 by 3 to 5 by 5 points. A series of 30 laser shots (or more to investigate the rock deeper) are used to collect spectra at a given point (Fig. 2). However, to avoid dust contamination, the first 5 spectra are removed before processing for quantification, and the last 25 spectra are averaged to give the mean chemistry of this point (Fig. 2).

In the case of large grains, such as phenocrysts or diagenetic concretions, the small footprint of the individual LIBS observations allows individual mineral chemistry to be obtained (e.g., Nachon et al., 2014, Sautter et al., 2015, Rapin et al., 2016). In contrast, in the case of mudstones/siltstones (<62 μm) and fine-grained sandstones (<250 μm), each point provides the average chemical composition of multiple grains (Mangold et al., 2017). A single point therefore provides a composition representative of the bulk chemistry. Here, the composition is averaged across all points in a given target (with a minimum of four points), further increasing the representativeness of the calculated bulk chemistry. In addition, this approach allows us not to bias the dataset with targets over which many points have been analyzed compared to targets with fewer points (e.g., Figure 2, Tab. 1).

This approach was previously applied to the mudstones and sandstones of Yellowknife Bay, where low deviations around mean values were observed over >500 analysis points collected (Mangold et al., 2015). At that location, an analysis of laser ablation cavities was done for both sandstones and mudstones (Arvidson et al., 2014). Results show that mudstones pits range from 0.2 to 0.6 mm, well above the grain size in these fine-grained rocks (<62 μm). Thus, each analysis point can be used as a bulk rock analysis for mudstones. Pits in sandstones are often larger, from 0.4 to 0.8 mm in the sandstones analyzed at Yellowknife Bay (Arvidson et al., 2014). At this scale, the laser spot on fine-grained to medium sandstones (<0.5 mm) still enable good average estimations, explaining for instance that the Gillespie lake sandstones did not show significantly larger standard deviations than the Sheepbed mudstones (Mangold et al., 2015). Over the 205 targets studied hereafter, only 5 correspond to medium to coarse sandstones, while the other 200 correspond to mudstones and fine-grained sandstones for which the average of four points is sufficient to provide a representative bulk chemistry.

A strength of LIBS is its ability to exclude points that probed diagenetic features instead of the bedrock itself. All points on resolvable diagenetic features have been removed by a systematic cross-analysis of RMI images, as, for example, point 5 in figure 2. The chemistry corresponding to point 5 (Tab. 1) displays a low total wt.% of oxides because this point is enriched in sulfur, which is an element that is difficult to detect, and so, it is not taken into account in the sum of major element oxides like most volatiles (H, C, P, etc.). The majority of points with low totals were removed after the RMI analyses. Many individual points have still low totals that we interpret as diagenetic features too small for visual determination. There is no definitive method to define the threshold (in total oxides wt.%) between the presence and absence of volatiles due to diagenetic phases, because the bedrock itself can display various abundances of volatiles (such as hydrogen inside clays, etc.). We choose here to use the maximum total of the major element wt.% oxides observed for targets for which diagenetic features were actually identified on images, found as ~90 wt.% in a couple of examples. While some amount of volatiles may still be present in targets with major element totals above 90 wt. %, this technique enables us to minimize the effect of diagenetic features enriched in volatiles, and thus provides a composition as close as possible to the bulk rock unaffected by diagenetic episodes.

By applying these criteria, 1660 points belonging to 205 different targets were retained in our analysis. The 205 bulk compositions were then normalized to total weight oxides of 100% to obtain volatile-free compositions (Tab. S1), which are useful for comparisons with other datasets, e.g., Mars average crust composition (Tab. S2). Note that this normalization has no consequence on the ternary diagrams shown later, which plots elements relative to the others.

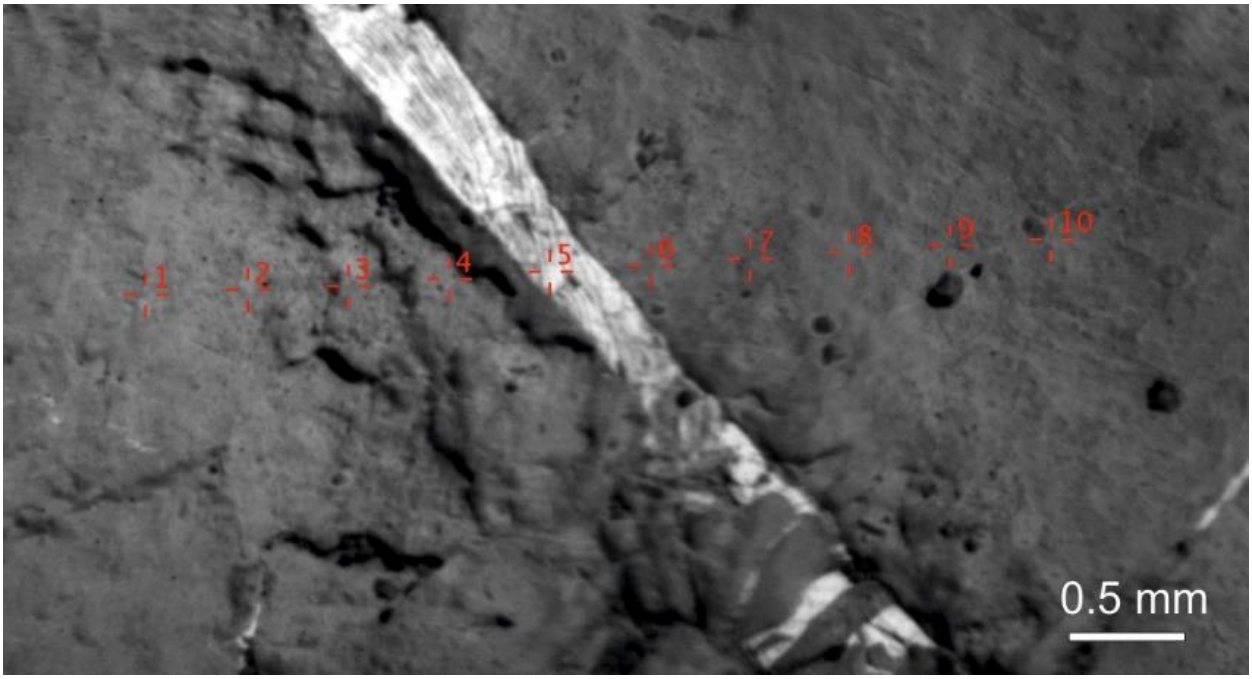

Fig. 2: Example of a RMI image of a Murray formation target (Upper Hadlock, sol 1505) crossed by a light-toned vein sampled on point 5. Table 1 displays the chemical results of this target.

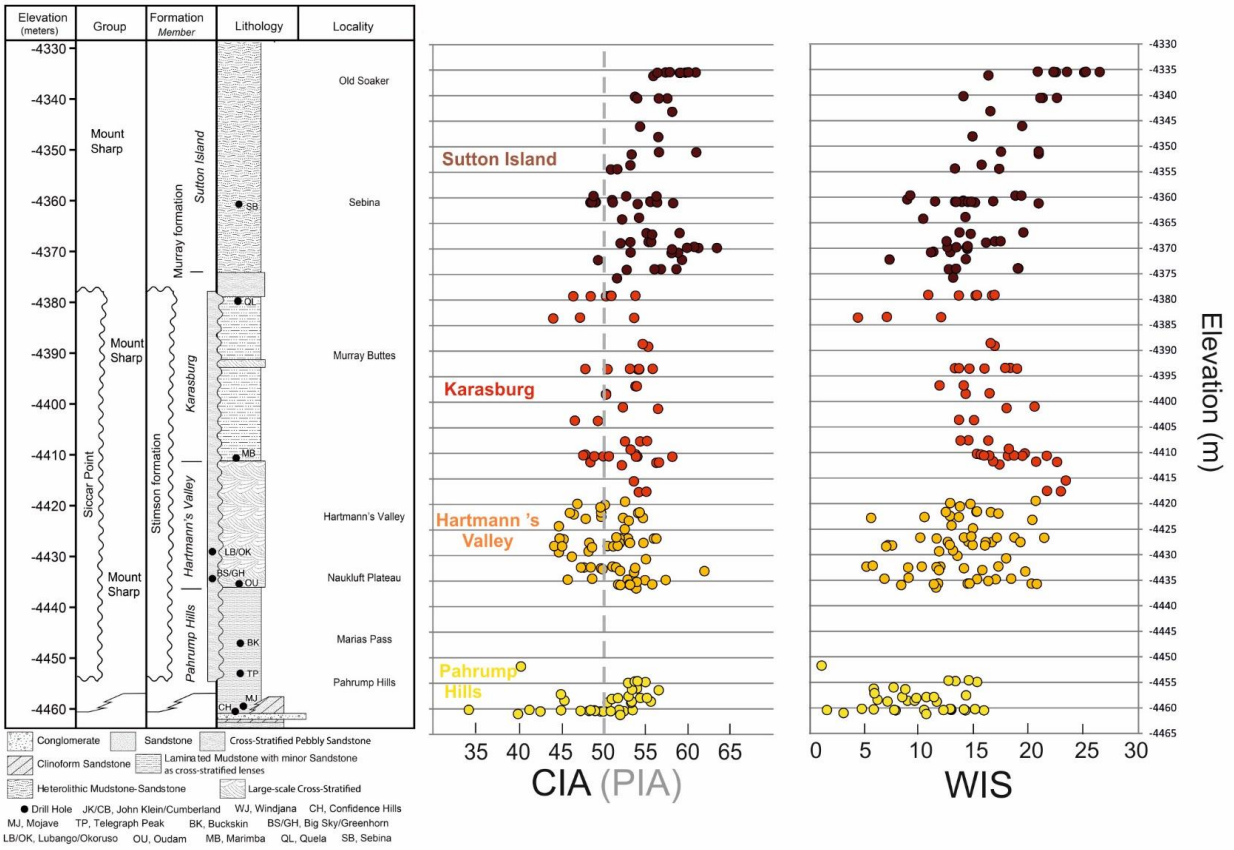

Fig. 3: (a) Stratigraphic column of the Murray formation highlighting the four areas of Murray used in this study. The gap above Pahrump Hills is related to the predominance of Si-rich outcrops of Murray formation and of the overlying Stimson formation. The stratigraphic framework shown here was established and refined through the efforts of the MSL sedimentology/stratigraphy working group (Fedo et al., 2017). (b) CIA plotted in filled circles along the stratigraphy for the four areas studied. PIA values are plotted next to CIA values in open circles. (c) WIS along the stratigraphy. WIS values calculated for starting composition corresponding to the average Mars crust. Starting from the average of Gale crater conglomerates would translate the diagram by 6% to the left.

2.2 CheMin data

CheMin collects X-Ray Diffraction (XRD) data using Co Kα radiation in transmission geometry (Blake et al., 2012). More details of instrument operation and sample analysis conditions can be found in in Bristow et al. (2018). Abundances of crystalline phases were determined by Rietveld analysis using Jade software. The results presented here are products of modeling that incorporate measured standards of clay minerals in addition to structures of crystalline phases (see Bristow et al., 2018 for more details). The abundances of amorphous components and poorly crystalline clay minerals are determined using the program FULLPAT (Chipera and Bish, 2002).

3. Geologic context and stratigraphy

From landing to sol 750, the traversed terrains are associated with the Bradbury group (Fig. 1). This formation consists of fluvial sandstones and conglomerates with local exposures of lacustrine mudstones. At Yellowknife Bay, the Sheepbed member of the Bradbury group corresponds to mudstones with basaltic chemical composition that are overlain by coarse sandstones divided into three members with basaltic composition as well (McLennan et al., 2014, Mangold et al., 2015, Anderson et al., 2015). At Kimberley, sedimentary rocks are potassic (up to 5 wt.% of K_2O) and consist of fine-grained sandstones and mudstones overlying conglomerates (Le Deit et al., 2017). In the Bradbury group, rocks are diverse and heterogeneous in grain size, in agreement with rocks derived mainly from alluvial/deltaic environments (Grotzinger et al., 2015), but relationships with the Mt. Sharp sequence are unclear due to the predominance of regolith and lack of contacts. Starting sol 750, at Pahrump Hills, rocks correspond to well-defined outcrops at the base of Mount Sharp that are exposed nearly continuously from there onto Mount Sharp on the orbital images, and have been named the Murray formation. As a consequence of this continuity and near-horizontal bedding, the stratigraphic section is described with elevation as a proxy for geologic time, allowing us to localize targets analyzed along the section (Fig. 3).

For the purpose of this study, the Murray formation was divided into four members from their geographic location and textural analysis (Fig. 1, Fedo et al., 2017). Part I of our study corresponds to the base of the Murray formation that was analyzed at the location named Pahrump Hills, a ~10-m high outcrop (sols 750-920, area I on Figs. 1 and 3) composed of interbedded lacustrine laminated mudstones and fluvial fine- to coarse-grained sandstones with local cross-bedding (Grotzinger et al., 2015). This location was analyzed with 36 ChemCam bedrock targets and 3 drill samples analyzed by CheMin (Confidence Hills, Mojave, Telegraph Peak, Figure 3).

After Pahrump Hills, the rover crossed hilly terrains of Marias Pass (sols 990-1050) and Bridger Basin (sols 1050-1150). At these locations, ChemCam analyses of the Murray formation were

discontinuous because the Murray formation was partially covered by lags and unconformably overlain by eolian cross-bedded fine-grained sandstones of the Stimson formation (Banham et al., 2016, 2018). Eolian sandstones from the Stimson formation formed well after the Murray formation (Banham et al., 2018), and are not included in this work for this reason. Outcrops of the Murray formation in these areas are locally enriched in silica (>60 wt.% SiO_2). XRD showed the presence of various phases of silica, including tridymite, which were interpreted as detrital components of silicic volcanic rocks in the drill target Buckskin (Morris et al., 2016). Light-toned halos (enriched in SiO_2 up to 80 wt.%) are frequently observed, suggesting a diagenetic episode due to Si-rich fluid circulation and related cementation (Frydevang et al., 2017). To avoid the bias that would be introduced by these diagenetically imprinted rocks on the weathering indices, we chose to exclude these few outcrops of the Murray formation from our study. This explains the gap in observation points between elevations -4450 and -4437 m in Fig. 3. Neither ChemCam data, nor CheMin mineralogy data of the Murray formation strata above this area indicate any further silica enrichment in bedrock apart from diagenetic halos (Bristow et al., 2018).

Part II of Murray formation (Fig. 2) is referred to as Hartmann's Valley member hereafter. The Hartmann's Valley member includes two areas at similar elevation (sols 1150-1270 and sols 1350-1400) separated by the Naukluft plateau composed of the overlying Stimson formation. Rocks in these two areas of Murray formation have a similar texture, with silt to very fine-sand sized grains, and local meter-scale cross-beds, interpreted as potential fluvial and eolian deposits (Fedo et al., 2017) (Fig. 3). The Hartmann's Valley member was analyzed using 63 ChemCam targets and 1 drill sample delivered to CheMin (Oudam, Figure 3).

Part III of our study is the Karasburg member (sols 1410-1468) which starts approximately at the southern edge of the plateau composed of the Stimson unit in a location with remaining residual buttes of the Stimson formation discontinuously capping the Murray formation (at a location named Murray buttes). The Karasburg member is composed of regularly mm-scale laminated mudstones interpreted as lacustrine deposits (Fedo et al., 2017). 46 ChemCam targets of the Karasburg member were analyzed as well as 2 drill holes (Marimba and Quela, Fig. 3).

Part IV of our study is the Sutton Island member (sols 1468-1550). Targets of this member are located in terrains with gentle slopes going upward, along Mt Sharp ascent route. In this area, the Murray formation consists of more heterolithic mudstones and sandstones (Figs. 1 and 3). Interpretations of the facies suggest that rocks were deposited in lacustrine and lacustrine-margin environments (Fedo et al., 2017) with evidence in the form of desiccation cracks indicating episodes of at least partial drying out (Stein et al., 2018). The Sutton Island member was analyzed using 60 ChemCam targets and 1 drill hole (Sebina, Fig. 3). A drill attempt, at Precipice, close to the desiccation cracks, was unsuccessful due to a mechanical fault.

A detailed description of stratigraphy and sedimentary facies is not the aim of this study. Further work on the facies will be the subject of detailed articles in the near-future. Nevertheless, we have analyzed the texture of targets using RMI images. A large majority of targets analyzed for this study are fine-grained sediments, with few or no grains visible at the usual scale of RMI images, i.e. 120-300 μm resolution for 3 pixel features, at 2 to 5 m distance (see Tab. 1 in Mangold et al., 2017). One exception is a horizon in the Pahrump Hills member where medium to coarse sandstones are observed in 5 targets. Independent, more in-depth assessments of the stratigraphy also point to the predominance of fine-grained sediments in Murray formation, either mudstones or fine-grained sandstones (Fedo et al., 2017, Rivera-Hernandez et al., 2018).

4. Chemical weathering indices

4.1 The Chemical Index of Alteration (CIA)

On Earth, many studies have attempted to estimate the degree of weathering based on chemical compositions of soils and sedimentary rocks. Weathering indices are based on the differential mobility of elements during alteration processes. Therefore, they reflect open-system weathering rather than isochemical alteration (Parker, 1970, Nesbitt and Young, 1982, Fedo et al., 1995, Meunier et al., 2013).

The Chemical Index of Alteration (CIA, see Methods) is the most commonly used index (Nesbitt and Young, 1982). It is based on the leaching of Ca, Na and K relative to Al. Al is an immobile major element in supergene alteration, thus taken as a reference. The CIA is calculated using the following relationship: $CIA = [Al_2O_3 / (Al_2O_3 + Na_2O + CaO^* + K_2O)] \times 100$, calculated in molar proportions. CaO* corresponds to CaO from silicates excluding CaO from carbonates, sulfates and phosphates. The filtering procedure explained in section 2 enables us to minimize the effect of these volatile-rich phases such as sulfates and phosphates, if present. Still, this correction is conservative, which means that our value of CaO is higher that the true CaO*. As a result, and because CaO is in the denominator of the equation, our calculated CIA values is underestimated compared to the actual CIA of each target.

In addition to the CIA, the Plagioclase Index of Alteration (PIA) (Fedo et al., 1995) is also calculated: $PIA=(Al_2O_3-K_2O)/(Al_2O_3+CaO^*+Na_2O-K_2O)$. This index helps to remove the effect of potential K-enrichment during burial and diagenesis (Fedo et al., 1995). CIA and PIA indices are represented in Fig. 3. PIA values are slightly higher than CIA values at Sutton Island by one or two CIA units at maximum, but overall PIA values are close to the CIA values of the corresponding targets. Thus, we focus most of the description on CIA values hereafter.

The point-to-point variations in these figures represents variations from one bedrock target to another bedrock target (thus from compositions averaged across an entire raster and not from one analysis point to another analysis point). In both indices, igneous rocks have CIA from 35 (ultramafic) to 50 (granite), and fully weathered rocks reach 100. A strength of the CIA is that it can be plotted as a vertical axis on a A–CN–K ternary diagram (Fig. 4a). This diagram is useful for comparing parent rocks and their weathering products because unaltered rocks and primary minerals plot with CIA≤50 below the plagioclase-K-feldspar join (50-50 line in Fig. 4a), and weathering products plot on a systematic trend predicted by thermodynamic and kinetic considerations. The A-CNK-FM diagram, where the alteration line joins the middle of the A-CNK line to the FM end-member, is provided for comparison (Fig. 4b).

Figure 4 displays two possible average source rocks for the sediments in the rocks of the Murray formation: (i) the widely-used average Mars crust composition (Taylor and McLennan, 2009) (Tab. S2) with a basaltic composition and a CIA of ~38, and (ii) the average composition of conglomerates analyzed by ChemCam at Gale crater, representing the least altered component of the sedimentary rocks analyzed at Gale crater (Mangold et al., 2016). Conglomerates are more felsic than Mars average crustal composition, explaining the higher CIA of ~45. At Yellowknife Bay, lacustrine mudstones (Sheepbed member) and fluvial sandstones have CIA values between 35 and 45 close to these two potential source rocks, a result that has been interpreted as a lack of open-system weathering (McLennan et al., 2014). In contrast, the CIA values of most Murray rocks plot well above 45 for all outcrops (Figs. 3 and 4).

CIA values display variations between the four areas considered (Fig. 3). The lowermost Pahrump Hills member appears slightly altered with an average of 49.8±5.1, in good agreement with values of ~50 reported there using APXS data (Hurowitz et al., 2017). The lowermost CIA values correspond to the group of coarser sandstones identified in this area. Hartmann's Valley member has CIA values similar to Pahrump Hills member (except one point at 61), with an average of 51.0±3.7.

The Karasburg member displays CIA values that are predominantly >50, with an average of 52.1±3.2, reaching up to 57. A difference with the underlying group is the much lower amount of values below 50. The Sutton Island member reports the highest group of CIA values with an average of 55.5±3.6 and several targets above 60, reaching up to 63. Overall, CIA values are increasing going up stratigraphy, and are above 50 for a large majority of the targets of the two upper members. The fact that a majority of points are above a CIA of 50 suggests that significant aqueous alteration took place.

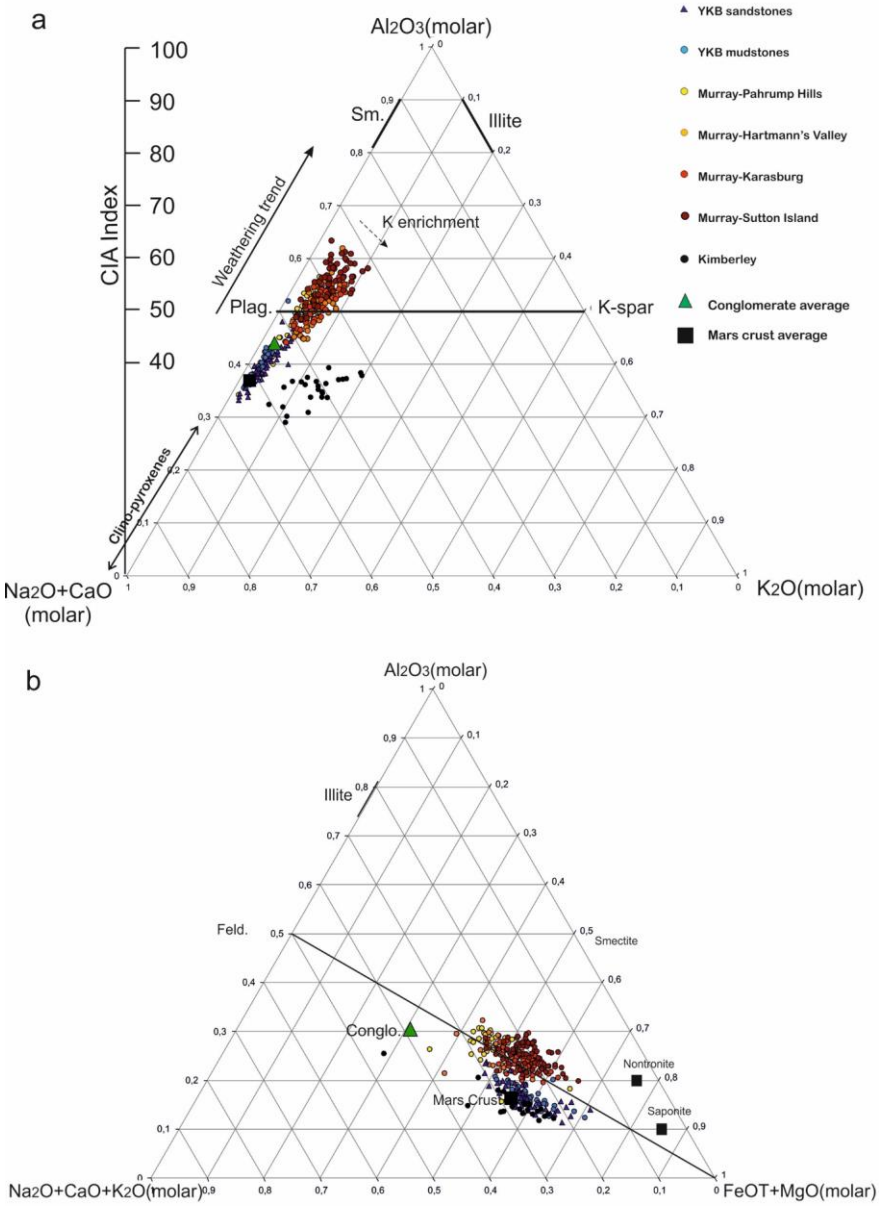

Fig. 4: (a) A-CN-K ternary diagram (molar values) with CIA values plotted on the vertical axis. Targets display many points above the 50-50 join, suggesting a limited contribution of primary minerals. Mars crust (black square) and average of Gale crater conglomerate (green triangle) represent potential source rock compositions with CIA values typical of unaltered rocks. Note that the drift towards higher potassium of Murray targets is correlated with higher CIA values. (b) Ternary molar A-CNK-FM diagram of the different sedimentary rocks of Gale crater. The line joining FM to the middle of the A-CNK join indicates the boundary between altered and non-altered rocks, the latter being below the line. As in Fig. 4a most Murray rocks plot above the alteration line though the evolution shown does not provide a clear trend suggesting a mixing of alteration phases.

332

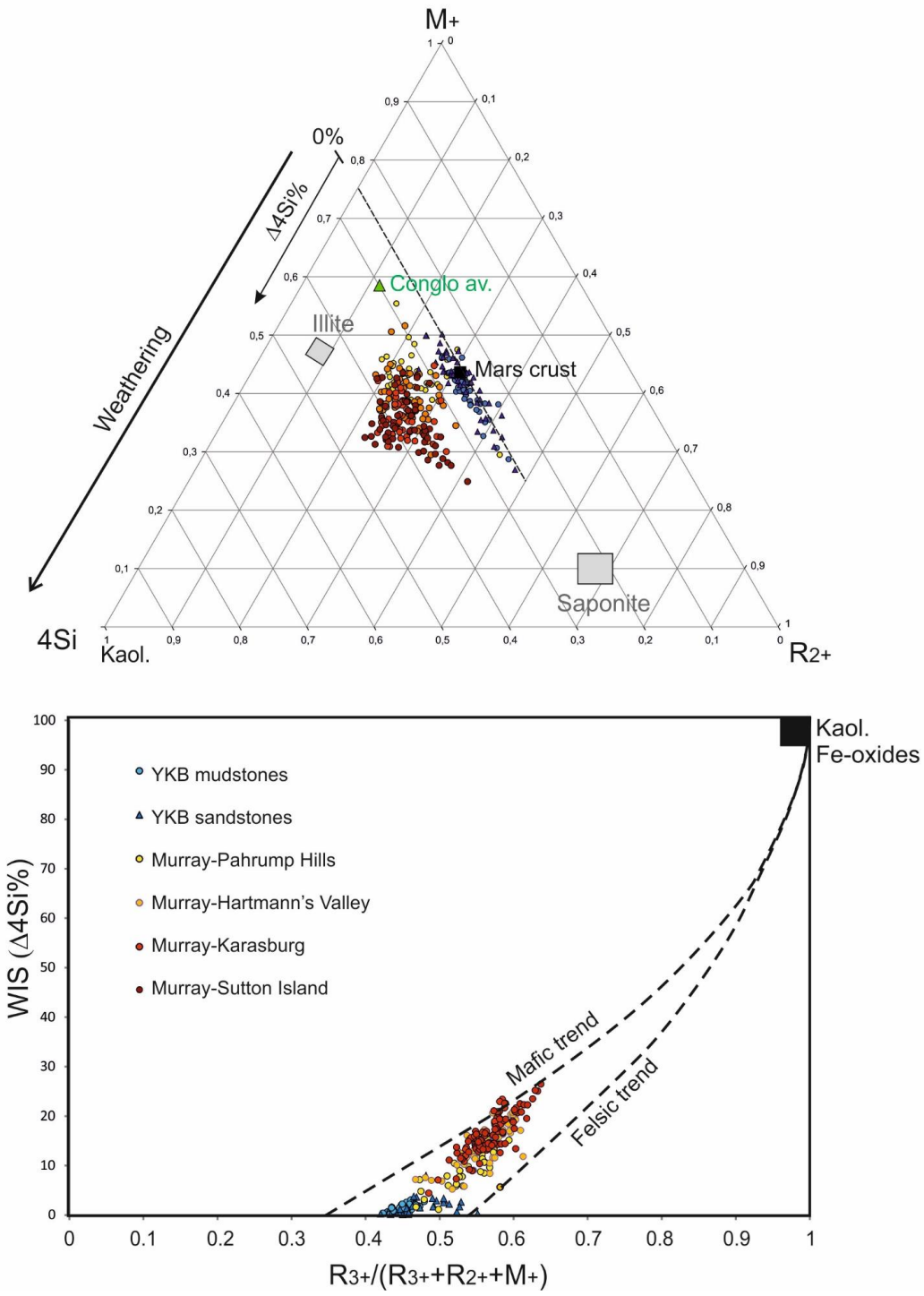

Fig. 5: (a) Ternary diagram of $M^{+}/R^{2+}/4Si$ showing the difference between potential source rocks composition and actual Murray formation composition to obtain the values of the WIS (difference of Δ4Si in %. see Methods). (b) Diagram showing $R^{3+}/(R^{3+}+R^{2+}+M^{+})$ vs Δ4Si% compared to the empirical trends observed for terrestrial mafic and felsic rocks.

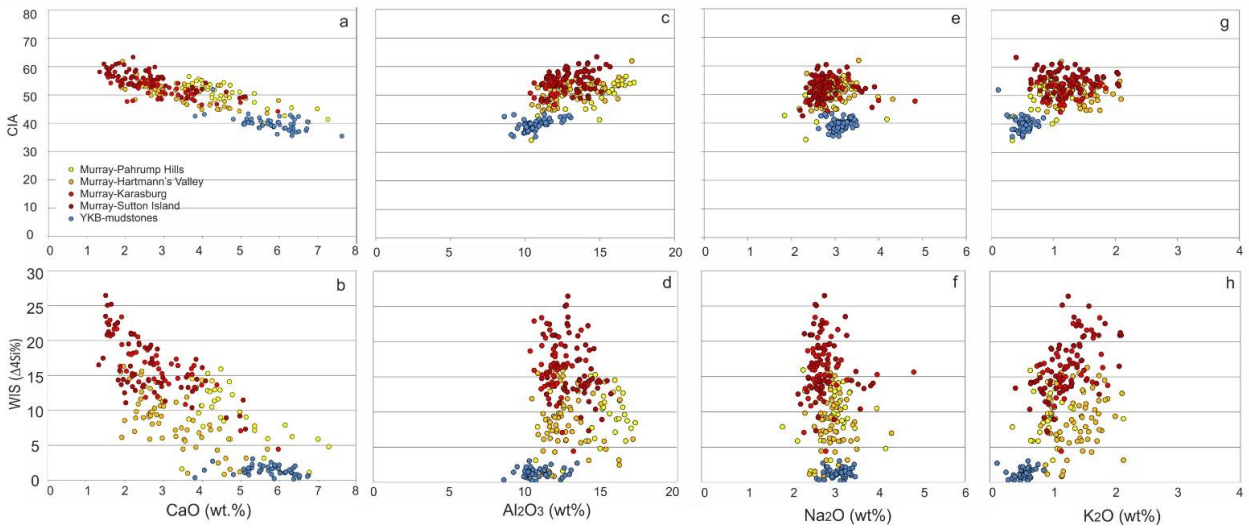

Fig. 6 : (a) Diagram plotting CIA vs CaO abundance showing a correlation between high CIA and low CaO. (b) Diagram plotting WIS and CaO abundance showing a similar relationship. (c) and (d) Same diagrams with Al_2O_3. (e) and (f) Same diagrams with Na_2O. (g) and (h) Same diagrams with K_2O. No obvious variations are observed with increasing weathering indices compared to that observed for CaO.

4.2 The Weathering Intensity Scale (WIS)

Most other weathering indices have usually good correlations with the CIA (Yang et al., 2006). However, the CIA does not take into account Si variations. For this reason, we have also used the Weathering Intensity Scale (WIS) (Meunier et al., 2013). The main components of the WIS are (1) *4Si*, which is the molar proportion of Si^{4+} divided by 4 to refer to the formula of phyllosilicates; (2) M^+, which is the sum of the molar proportion of alkali and earth alkali elements (Na^++K^++2Ca^{2+}); (3) R^{2+}, which groups the bivalent elements (Mg^{2+}+Fe^{2+}+Mn^{2+}), and (4) R^{3+} which groups the trivalent cations (Al^{3+} + Fe^{3+}). This method enables to sort the mobile elements (M^+ and R^{2+}) from the elements stable in soils (R^{3+}). For the R^{2+}, we neglect the effect of Mn^{2+} because it is not systematically taken into account in the quantification of major elements by ChemCam. High Mn values (>3%) have been observed locally on Mars in fracture fills (Lanza et al., 2014), but average values are ca. 0.4% corresponding to a minor shift from the much larger contribution of Fe and Mg (totaling >25 wt.% for most targets).

The M^+, *4Si* and R^{2+} amounts are first normalized to 100% (see Meunier et al., 2013) and plotted in a ternary diagram (Fig. 5a). The Δ4Si% (referred to as WIS for simplicity) is then a parameter

varying from 0 to 100% measured by the difference between the compositions of unweathered and weathered samples : $\Delta 4Si\% = ((4Si_{altered\ rock} - 4Si_{unaltered\ parent\ rock}) * 100)/(100 - 4Si_{Unaltered\ parent\ rock})$. It can be visualized on the ternary diagram by the distance from the reference unaltered source rock (Fig. 5a). Any index aiming to measure weathering must also take into account the progressive concentration of trivalent chemical components (R^{3+})(Meunier et al., 2013). The second diagram (Fig. 5b) plots the $\Delta 4Si\%$ obtained versus the increase in trivalent cations calculated from the ratio $R^{3+}/(R^{3+}+R^{2+}+M^{+})$.

The R^{2+} and R^{3+} in the WIS calculation requires an estimation of the Fe^{2+}/Fe^{3+} ratio, which is not directly accessible from ChemCam data. It was recognized as a weakness of the method (Meunier et al., 2013). CheMin XRD data have been used locally to estimate this ratio in the Murray mudstones, at the drill hole Marimba (Tab. 2). Result shows a strong predominance of the ferric oxides with Fe^{2+}/Fe^{3+} (molar)=0.00301/0.0509=0.059. Given large assumptions on the mineralogy of ferrous minerals and the fact that the amorphous component cannot be determined by this method, we have used a conservative value of Fe^{2+}/Fe^{3+} of 0.1. Comparison of chemistry and mineralogy in previous drill holes has argued for the presence of ferrihydrite in the amorphous component (Dehouck et al., 2017) suggesting a large part of the iron of this component is indeed ferric, so it would not change this ratio significantly. We have also performed tests at various Fe^{2+}/Fe^{3+} ratio to estimate the impact of these variations to the WIS, showing that the difference in $\Delta 4Si\%$ is minor whatever the Fe^{2+}/Fe^{3+} ratio taken (Fig. S1).

The ternary diagram using the three first components M^{+}-4Si-R^{2+} shows that the targets from the Karasburg and Sutton Island members plot away from the two potential source rocks yielding WIS values of up to 26% at Sutton Island using Mars crust composition as the initial source, or 20% taking the conglomerate average composition as the source. These results are consistent with those using the CIA although the WIS calculation includes SiO_2. The diagram plotting the WIS versus the trivalent cations shows a progressive increase similar to the empirical trends observed for terrestrial felsic and mafic rocks. The trends are significant in both diagrams although the alteration is relatively limited and far from reaching the kaolinite end-member. In contrast, Bradbury group mudstones (Sheepbed member) do not show any substantial increase in the WIS (Fig. 5), in agreement with their low CIA (Fig. 4). For simplicity, we have used the same Fe^{2+}/Fe^{3+}ratio for all targets, although it creates an overestimation of the X-axis of the unaltered targets, which are naturally more ferrous. This assumption explains why the trend provided by all targets is slightly shifted between felsic and mafic from the empirical lines drawn in Fig. 5 (bottom).

4.3 Chemical variations in relation to alteration indices

Leaching of sodium, calcium, or potassium, or a combination of these elements, is needed to explain CIA values greater than 50. The CaO abundance is low in all Murray formation (2-5 wt.%, Tab. S1) compared to average Mars crust (at ~7 wt.%, Tab. S2). Calcium is also the only cation that decreases significantly with higher CIA and WIS (Fig. 6). CaO abundance is as low as 1.5-2.5 wt.% for targets with CIA>55, by comparison with rocks displaying CIA<50 that have CaO>4 wt.% (Fig. 6a). CaO shows a progressive decrease from Pahrump Hills (4.8±1.2 wt.% in average, see Tab. S1) to Hartmann's Valley (3.3±1.0 wt.%) then Karasburg (2.8±0.9 wt.%) and Sutton Island (2.6±1.0 wt.%). In contrast to CaO, no obvious trend is observed with the other elements used for the CIA calculation (Fig. 6c, 6e, 6g), although K_2O displays a slight increase with CIA. Al_2O_3 displays a variability in abundance that may be related to natural variations in clastic sedimentation processes. These variations do not show a correlation with the highest CIA values, showing that these variations in Al are not the cause of the high CIA values, which is based instead on trends in cation abundances within each rock.

Similarly, values of WIS>20% correspond to low abundance of CaO (<2.5 wt.%, Fig. 6b), and not of other elements, confirming the trend observed with the CIA with an index less dependent on calcium. A comparison between the CIA and the WIS (Fig. 3) also shows that the Karasburg and Sutton Island members are those where the alteration is the most developed for both alteration indices. The WIS exhibits slightly larger variations, indicating a diversity that could be related to local variations in the intensity of alteration.

5. Results from mineralogy

CheMin analyzed three drill samples at Pahrump Hills (Confidence Hills, Mojave and Telegraph Peak, Rampe et al., 2017), one at Hartmann's Valley (Oudam), and three in the two upper members (Marimba, Quela and Sebina) where both the CIA and WIS are the highest (Fig. 3, Tab. 3). In these latter three drill samples, CheMin data indicate the presence of abundant clay minerals (~16 to 28 wt.% of the whole rock) (Tab. 3). Clay minerals in these three samples are interpreted as a mixing of phases such as di-octahedral smectites (with Al^{3+} and Fe^{3+}) and tri-octahedral smectites (with Mg^{2+}). The presence of these phases is consistent with the enhanced alteration observed from chemistry (Bristow et al., 2018). By comparison, drill samples in the Pahrump Hills and Hartmann's Valley members do not contain large proportions of phyllosilicates (~3%), suggesting a lower imprint of alteration – at this point, either from detrital input or *in situ* alteration, or both -, in agreement with the lower CIA and WIS in these areas.

The three uppermost drill samples also display a lower proportion of primary minerals (olivine, pyroxene, plagioclase and alkali feldspar) than the previous drill samples. Plagioclase is the most abundant primary mineral everywhere, but it is present in lower proportion in the three upper

drill holes (10 to 14 wt.%) than in the four lower drill ones (20 to 27 wt.%) (Tab. 3). Mafic minerals are in very low proportion in the three upper drill holes, with no olivine and pyroxenes representing only ~0.7 wt.% at Marimba, 2.7 wt.% at Quela and 2.8 wt.% at Sebina, compared to 5 to 13 wt.% of pyroxenes (and 1% of olivine) in the four previous drill holes. These trends are still valid when removing the amorphous component from the balance, i.e. the low abundance of primary minerals in the three upper drills is not due to a higher proportion of amorphous component. Thus, CheMin data display an increase in clay mineral abundances going up section where the alteration indices are the highest.

6. Discussion

6.1 Alteration versus provenance effects

The increase in clay minerals, decrease in primary mafic minerals and decrease in CaO abundance are all specific to the two upper members (Karasburg and Sutton Island), which display the highest alteration indices, thus favoring a role of enhanced alteration up section. Before discussing the origin of the potential alteration (sections 6.2 and 6.3), we discuss hereafter potential links between mineralogy and chemistry to understand if these trends are related to provenance or alteration, or both.

A potential explanation of the low calcium abundance up section is that this element could have been leached from Ca-bearing minerals, such as plagioclase and clinopyroxene. We can test this hypothesis by comparing the mineralogy and chemistry of the relevant locations. It must be recalled, nevertheless, that drill holes are not numerous, and so, do not enable a statistically representative comparison between chemistry and mineralogy.

Plagioclase is the dominant primary mineral in all drill samples, but with lower proportions in the three upper drill holes. We can estimate the variations in CaO abundance linked to these variations of mineralogy, assuming a plagioclase stoichiometry of An40, as estimated among the Pahrump Hills member drill holes (Morrison et al., 2017). The CaO abundance due to 20-27 wt.% of plagioclase observed from Confidence Hills to Oudam corresponds to an abundance of CaO of 1.7-2.3 wt.%. By comparison, the 10 to 14 wt.% plagioclase observed in the three upper drill samples represents 0.8-1.2 wt.% of CaO. Thus, net losses of CaO are in the range of 0.5-1.5 wt.%. These values are in agreement with the decrease in CaO abundance recorded by ChemCam, from the Pahrump Hills (4.8 wt.%) to the Sutton Island member (2.6 wt.%), although not sufficient to explain all the CaO loss.

These differences in composition may be due to variations in provenance rather than alteration. In such a hypothesis, a lower proportion in plagioclase and alkali feldspar in the three upper drill

holes should be related to more mafic source rock(s). However, the very low proportion of pyroxene and lack of olivine does not argue for a more mafic source rock there, thus ruling out this possibility. The lower amount of plagioclase could instead be related to a partial dissolution of this mineral as highlighted by the higher CIA values, which is the most sensitive index to this process. Assuming a partial dissolution of plagioclase, this process should be visible by a coupled decrease in sodium, which is not clearly observed (Fig. 6). Nevertheless, plagioclase minerals are known to dissolve incongruently, which means that the ions in the mineral lattice do not dissolve according to their stoichiometry, enabling calcium to be leached preferentially (e.g., Wilson, 2004). Note that a lower plagioclase abundance due to provenance effects would lead to a corresponding decrease in sodium.

A striking observation is that the three upper drill holes display the lowest proportion of mafic minerals ever observed by Curiosity (<2.8wt% of pyroxene, no olivine). A decrease in the proportion of clinopyroxene can also contribute to the decrease in CaO abundance recorded by ChemCam. The pyroxene structure in these drill holes is difficult to determine due to its low abundance (Bristow et al., 2018). So, we cannot provide a proper estimate of its contribution to the CaO abundance. Nevertheless, drill holes of the lower Murray members and of the Bradbury group include pigeonite, augite and some proportion of orthopyroxene (Morrison et al., 2018). In the Pahrump Hills member, the Confidence Hills drill hole contains pigeonite and orthopyroxene (with no Ca) accounting for 14 wt.% of the crystalline phases and augite accounting for 12 wt.% of the crystalline phases (Morrison et al., 2018). Note nevertheless that the augite stoichiometry was not computed and assumed to be similar to the Bradbury group with 18 wt.% CaO (Morrison et al., 2018). Accounting for the amorphous component comprising 35 wt.% at Marimba, the abundance of CaO corresponding to augite would then be ~1.4 wt.%. This value is of the same magnitude than the 0.5-1.5 wt.% of CaO loss from plagioclase for a total loss of 1.9-2.9 wt.%, consistent with the difference of CaO abundance (2.2 wt% in average, see Tab. S1) measured by ChemCam between Pahrump Hills and Sutton Island (Fig. 6a, b).

The low proportion of mafic minerals in the drill holes from upper stratigraphic members can be due to provenance or sorting effects instead of dissolution. However, pyroxenes are common minerals of the Mars crust, both in Noachian or younger terrains (e.g., Poulet et al., 2009), and were identified in all previous drill samples, in much higher proportions (>10 wt.%) than in the three drill samples considered (Morrison et al., 2018). In addition, the chemistry does not point towards an increase in felsic or alkali components (K, Na) as it was observed in the initial part of the mission (Sautter et al., 2015, Mangold et al., 2016). Indeed, there is no coupled increase in Si, Al and K, and CheMin indicates that feldspars are not in higher proportion (alkali feldspar abundance is actually lower up section in CheMin analyses, Tab. 3). These observations show that a more felsic parent composition is not a valid explanation for the low proportion of mafic minerals. In addition, sorting of grains in fine-grained sedimentary rocks has been shown to

increase the proportion of dense, resistant mafic minerals rather than decrease it (Siebach et al., 2017), a conclusion inconsistent with an effect of sorting in the studied locations. Thus, the low proportion of pyroxene in the three drill holes of Karasburg and Sutton Island members suggests that their partial dissolution contributed to the loss of CaO.

Dissolution of pyroxenes would also result in Mg and Fe leaching too. While MgO is present at ~5 wt.% abundance in the Karasburg and Sutton Island members (Tab. S1), this value is lower than in sedimentary rocks analyzed previously in the mission (~8 wt.% in the Sheepbed member of the Bradbury formation, at Yellowknife Bay, e.g., McLennan et al., 2014). In addition, there are not enough primary minerals remaining to explain the abundance of MgO: the abundance of 2.8 wt.% pyroxene would translate to <1 wt.% MgO. In contrast, magnesium is present in the tri-octahedral clay minerals (saponite) detected at Marimba, Quela and Sebina (Bristow et al., 2018). It is known on Earth that smectites formed during weathering are able to incorporate structural magnesium in octahedral sites while calcium cannot go into these sites (e.g., Nesbitt and Wilson, 1992), and can only be present as interlayer potentially explaining why calcium shows a net loss. By comparison to Mg, Fe is less mobile and is known to remain in soils during weathering. The high proportion of hematite (~6-7 wt.%) in the three drill holes could correspond to a byproduct of alteration (including diagenesis). In addition, both Fe and Mg are potentially present in the amorphous component as well, in phases such as hisingerite and ferrihydrite as it has been deduced from data earlier in the mission (Dehouck et al., 2014, 2017). From Tab. 2, we can deduce that only ~8 wt.% of FeO_T is taken by crystalline phases identified by CheMin (especially hematite), therefore suggesting that the remaining ~10 wt.% are concentrated in the amorphous component.

Possible variations in the composition of the amorphous component from one drill sample to another could have an impact on the chemistry analyzed by ChemCam. For instance, Al-rich phases (such as allophane) could have an impact on the CIA calculation by increasing the Al_2O_3 abundance, while both Al and Si could have an impact on the WIS. So far, no Al-rich amorphous component has been identified (Dehouck et al., 2017, Morrison et al., 2018). The comparison between chemistry and mineralogy (Tab. 2) points towards an excess of FeO relative to the low abundance of identified mafic minerals, suggesting an iron-rich amorphous component, as in Dehouck et al., 2017. In this case, variations in the proportion of the amorphous component would have little impact on the CIA calculation.Concerning Si, no opal has been detected in the drill holes of the two upper members (Tab. 3), suggesting that these locations are distinct from the high-silica locations analyzed on sols 1000-1100, with the exception of the local presence of Si-rich diagenetic halos that have been analyzed punctually and clearly postdate the rock deposition as they cross also the overlying Stimson unit (Frydenvang et al., 2017). The good correlation between WIS and CIA, calculated using different cations, also points towards the limited influence of amorphous phases on the variability of these indices, although more work on

the amorphous component should be done to understand its origin and role in the processes of alteration.

In summary, with limitations due to the lack of knowledge of the amorphous component and the limited number of drill holes, the high CIA and WIS targets in Karasburg and Sutton Island are consistent with a change in mineralogy related to a significant alteration by aqueous processes with partial dissolution of primary minerals such as pyroxene and plagioclase.

6.2 Diagenetic imprint

Post-depositional alteration during diagenesis may have modified the mineralogical assemblages. With that regard, another chemical trend observed is the slightly higher K_2O abundance (up to 2 wt.%) observed on the ternary diagram trending away from the A-CN axis (Fig. 4a). The Kimberley sandstones are plotted for comparison in Fig. 4a showing that these fluvial sandstones with anomalously high K-spar abundance (Le Deit et al., 2016, Treiman et al., 2016) (up to 5 wt.% K_2O) cannot explain this trend by mixing or source rocks effects because for Murray formation rocks the trend towards higher K_2O is correlated with the higher CIA

In contrast, illite and interlayered illite/smectite are possible candidates for such an enrichment; they commonly form during burial and diagenesis (e.g., Fedo et al., 1995). It would also be in agreement with modeling of the burial of Mount Sharp sediments (Borlina et al., 2015). CheMin observations do not favor illite as the main phyllosilicate present (Bristow et al., 2018). The K_2O abundance at Marimba is ~1.0 wt.% based on ChemCam data (Tab. S1). Yet, the modeled proportion of sanidine in CheMin pattern is only 2.4±0.6 wt.% at Marimba (and less at Quela and Sebina; Bristow et al., 2018) while jarosite is below detection limit (<1%). The equivalent proportion of K_2O of a sanidine (~14 wt.% as an average of the four lower Murray drills, Morrison et al., 2018) corresponds only to ~0.4 wt% K_2O, thus not accounting for all the potassium present at Marimba. So, a contribution of illite or interlayered illite/smectite is possible, although difficult to demonstrate.

The Plagioclase Index of Alteration (PIA) was proposed to correct for the addition of K_2O during burial (Fedo et al., 1995) (Fig. 3). PIA values are usually slightly above CIA for Karasburg and Sutton Island, suggesting the actual CIA values before burial were slightly higher, but they remain close to CIA suggesting minor contributions. Thus, variations in K_2O cause minor effects on the CIA, and diagenesis is unlikely to be the origin for the high CIA values.

6.3 Origin of the alteration observed

Both alteration indices, CIA and WIS, show evidence for substantial alteration of the Murray formation. The CIA ranges from 50 to 63, strongly favoring that the alteration occurred in an open-system, contrasting with the closed-system alteration observed in Sheepbed member mudstones (Bradbury group at Yellowknife Bay), with CIA of ~40 (McLennan et al., 2014). Indeed, closed-system alteration, such as found in local hydrothermal circulation or deep diagenesis, does not increase the CIA index (remaining below the 50-50 line on figure 4). However, these chemical indices usually represent a combination of weathering in the source region, during transport, and in depositional areas (McLennan, 1993, Fedo et al., 1995, Cox et al., 1995, Nesbitt and Young, 1996, Yang et al., 2006, Garzanti et al., 2013). Thus, it remains debatable whether this alteration predates or coincides with the deposition of the fine-grained sediments within Gale crater.

On one hand, altered source rocks are possible contributors to the high alteration indices. In this case, the clay minerals present in high CIA Murray rocks are predicted to have a detrital origin. Their presence could have been favored by grain-size sorting during depositional processes with limited alteration during lake activity. Alteration of source rocks could have been in the form of crustal or hydrothermal alteration related to the Gale impact crater, either by exhumation of deep crustal rocks or by hydrothermal activity immediately after its formation. However, no high-T secondary minerals indicative of hydrothermal conditions have been detected by CheMin in the three upper drill holes or in previous clay-rich samples (Bristow et al., 2015). Only some of the small fraction (3 wt.%) of clay minerals at Oudam (Hartmann's Valley) may be interpreted as of pyrophyllite/talc type mixed within eolian deposits (Bristow et al., 2018). In contrast, the presence of substantial proportions of di-octahedral phyllosilicates in the three upper drill holes is consistent with an open-system, low-T alteration. Here too, the low proportion of mafic minerals, usually sorted in higher proportion in finer-grained sediments (Siebach et al., 2017) does not favor a pure detrital assemblage as these minerals should have been transported from unaltered sections of the crater rim as observed in the Bradbury group. Thus, we do not favor the scenario of rocks altered hydrothermally before or immediately after Gale crater's formation. Nevertheless, it is still possible that weathering processes postdating Gale crater's formation could have reprocessed hydrothermal clays into the smectites that are observed, or that weathering affected source rocks after the emplacement of Gale crater but prior to the formation of the lake deposits. On the other hand, some observations argue for in-situ weathering linked to fluvial and lacustrine processes. The depletion of calcium interpreted by leaching is consistent with observations of calcium sulfate cements (Newsom et al., 2017, Vaniman et al., 2017). The Old Soaker outcrop (Sutton Island member), displays evidence for desiccation cracks that demonstrate a subaerial exposure of these sediments (Stein et al., 2018). We have no constraint on the frequency, duration, and repetition of such episodes, but the presence of these cracks requires that the lake was shallow enough to permit local subaerial exposure of sediments where additional weathering could have occurred, thus providing a possible explanation for targets that display higher alteration in this section of Murray formation.

In summary, the weathering process(es) evidenced in this study could have taken place in the source region, during transport or after deposition, or at these three stages and coevally in the whole basin, and we cannot give more precision about this activity. However, we can exclude the possibility that the observed mineralogy and chemistry consists only of detrital material of hydrothermally altered rocks transported and deposited in a lake without further alteration.

6.4 Climate conditions recorded by alteration indices

Several terrestrial studies have shown the link between climate and variations in alteration indices. Although the WIS has not been studied at the same level of detail as the CIA, maximum values of the WIS of 20-25% are in agreement with conditions required by CIA of ~55-60 (Meunier et al., 2013)(Table 4). Studies in the Arctic (Nesbitt and Young, 2016) and in Antarctica (Salvatore et al., 2013) have shown that a cold and dry climate is unlikely to generate alteration indices >50. Analyses of loess deposits in China and southeastern Europe indicate a CIA index of 60-65, after semi-arid conditions during Pleistocene glacial-interglacial climates, with active weathering during wet seasons over geologically long durations (Yang et al., 2006, Buggle et al., 2011). In contrast, empirical laws extracted from a database of US soils (Sheldon et al., 2002) show that a CIA of ~55-60 would translate into a temperate climate with high annual precipitation of ~600 mm. Alteration indices vary a lot according to parameters such as local climate, elevation, bedrock composition and texture, not enabling the determination of a unique environment at a given index value. In particular, felsic rocks such as the terrestrial continental crusts have higher starting values of CIA (unaltered rocks ca. 45-50, e.g. Nesbitt and Young, 1996, Fedo et al., 1995) than starting values for mafic rocks (unaltered rocks ca. 35-40, e.g. Babechuk et al., 2014) as observed for Mars average crust, Sheepbed mudstones (Bradbury group) or soils, which all range from 35 to 40 (McLennan et al., 2014) as shown in Figure 4 and Table 4. Thus, at a similar CIA value, alteration is underestimated for mafic rocks (which are found predominantly in Gale crater sediments), supporting the idea that the Murray sediments are significantly altered. For instance, basaltic sediments analyzed in Iceland, a currently wet and cold climate, have been estimated at only 45-50, despite the high rate of precipitation in this region (Thorpe et al., 2017).

In summary, climate conditions required to explain our observations involve substantial liquid water at the surface that a cold, dry climate cannot explain, although a specific climate cannot be specified. Previous results from Curiosity indicated the presence of substantial fluvial and lacustrine sedimentation, in what appeared to be relatively cold and dry environment according to geochemical markers, i.e. CIA values at ~40 (Grotzinger et al., 2014, McLennan et al., 2014). The finding of substantial weathering from chemical variations fills a gap in this history, and suggests that the lacustrine activity was coupled with, or was preceded, by a period of open-system weathering.

7. Conclusions

From Sol 750 to 1550, the Curiosity rover documented >130 m of stratigraphy during its 6 km traverse of fine-grained sedimentary rocks of the Murray formation, at the base of Mt Sharp. ChemCam data were used to estimate the level of weathering in these sedimentary rocks. Both the Chemical Index of Alteration (CIA) and the Weathering Index Scale (WIS) indicate a progressive increase in alteration up section, in the range of 55-60, locally reaching CIA values of 63 and WIS of 25% contrasting with limited weathering observed in the primary phase of the mission (McLennan et al., 2014). To date, alteration indices of this magnitude have never been observed in-situ on Mars. This enhanced alteration is consistent with abundant clay minerals of both di-octahedral and tri-octahedral nature (Bristow et al., 2018). The increase in CIA and WIS values is coupled with a decrease in calcium abundance, suggesting partial dissolution of clinopyroxene and plagioclase, which both are observed in lower abundances in the drill holes up section. In contrast to deep diagenetic or hydrothermal processes that occur in closed systems, these observations indicate alteration in an open system with the presence of liquid water, at or near the surface.

Acknowledgements

We acknowledge the two reviewers for their insightful comments. This research was carried out with funding from the Centre National d'Etudes Spatiales (CNES) and the Agence Nationale de la Recherche (ANR) under the program ANR-16-CE31-0012 entitled *"Mars-Prime"*. Work in the United States was carried out under contract from NASA's Mars Program Office. The data reported in this paper are archived at the Planetary Data System, accessible at http://pds-geosciences.wustl.edu/missions/msl/index.htm. J.F. acknowledges the support from the Carlsberg Foundation. Author contributions: N.M. analyzed ChemCam data and wrote the text. E.D., C.F., S.M.M and M.S. provided input on stratigraphy and alteration indices on Earth. E.D., O.F. J.F., O.G., J.H., L.L.D., S.M., P.M., H.E.N., W.R., F.R-H, R.W participated in ChemCam data acquisition and processing. C.A, T.B., S.M., E.R., R.D participated to the processing and analyses of CheMin data.

Supplementary material

Supplementary material related to this article can be found in the accompanying file.

References

Anderson R. B. and Bell III J. F., 2010. Geologic mapping and characterization of Gale Crater and implications for its potential as a Mars Science Laboratory landing site, Int. J. Mars Sci. Exploration, 5, 76-128.

Arvidson, R. E., P. Bellutta, F. Calef, A. A. Fraeman, J. B. Garvin, O. Gasnault, J. A. Grant, J. P. Grotzinger, V. E. Hamilton, M. Heverly, K. A. Iagnemma, J. R. Johnson, N. Lanza, S. LeMouélic, N. Mangold, D. W. Ming, M. Mehta, R. V. Morris, H. E. Newsom, N. Rennó, D. Rubin, J. Schieber, R. Sletten, N. T. Stein, F. Thuillier, A. R. Vasavada, J. Vizcaino, and R. C. Wiens, 2014, Terrain physical properties derived from orbital data and the first 360 sols of Mars Science Laboratory Curiosity rover observations in Gale Crater, J. Geophys. Res. Planets, 119, doi:10.1002/2013JE004605

Babechuk, M. G., Widdowson, M., Kamber, B.S., 2014. Quantifying chemical weathering intensity and trace element release from two contrasting basalt profiles, Deccan Traps, India, Chemical Geology, 363, 56-75.

Banham, S.G., Gupta, S., Rubin, D.M., Watkins, J. A., Sumner, D.Y., Grotzinger. J.P., Lewis, K.W., Edgett, K.S., Edgar, L.A., Stack, K.M., 2016. Reconstruction Of An Ancient Eolian Dune Field At Gale Crater, Mars: Sedimentary Analysis Of The Stimson Formation, 47th Lunar Planet. Sci. Conf., #2346.

Banham, S.G., S. Gupta, J. Watkins, K. Edgett, D. Sumner, J.P. Grotzinger, K. Lewis, L. Edgar, K. Stack, R. Barnes, J. Bell, D. Mackenzie, R. Ewing, M.G.A. Laporte, N. Stein, F. Rivera-Hernandez, A. Vasavada, 2018. Ancient Martian aeolian processes and palaeomorphology reconstructed from the Stimson formation on the lower slope of Aeolis Mons, Gale crater, Mars. Sedimentology, 65 (4), 993-1042, https://doi.org/10.1111/sed.12469.

Blake D., et al., 2012. Characterization and calibration of the CheMin mineralogical instrument on Mars Science Laboratory. Space Sci. Rev. 170, 341–399.

Borlina C. S., Ehlmann, B. L., Kite, E. S., 2015. Modeling the thermal and physical evolution of Mount Sharp's sedimentary rocks, Gale Crater, Mars: Implications for diagenesis on the MSL Curiosity rover traverse, J. Geophys. Res., 120, 1396-1414.

Bristow T. F. et al., 2015. The origin and implications of clay minerals from Yellowknife Bay, Gale crater, Mars. Am. Mineral. 100, 824-836.

Bristow T. F. et al., 2017. Surveying Clay Mineral Diversity In The Murray Formation, Gale Crater, Mars. 48th Lunar Planet. Sci. Conf., #2462.

Bristow, T. F. et al., 2018. Clay mineral diversity and abundance in sedimentary rocks at Gale Crater, Mars, Scientific Advances, in press.

Buggle B., Glaser, B., Hambach, U., Gerasimenko, N., Markovic, S., 2011. An evaluation of geochemical weathering indices in loessepaleosol studies, Quat. Inter., 240, 12-21.

Chipera S. J. and D. L. Bish, FULLPAT: A full-pattern quantitative analysis program for X402 ray powder diffraction using measured and calculated patterns. J. Appl. Crystallogr. 35, 744–403 749 (2002).

734 Clegg S. et al., 2016. Recalibration of the Mars Science Laboratory ChemCam instrument with an expanded
735 geochemical database, Spectrochemica Acta Part B, 129, 64-85.

736 Cox, R., Lowe, D.R., Cullers, R.L. 1995. The influence of sediment recycling and basement composition on
737 evolution of mudrock chemistry in the southwestern United States. Geochimica et Cosmochimica Acta, 59,
738 2919–2940.
739
740 Dehouck, E., S. M. McLennan, P.-Y. Meslin, and A. Cousin (2014), Constraints on abundance, composition,
741 and nature of X-ray amorphous components of soils and rocks at Gale crater, Mars, J. Geophys. Res.
742 Planets, 119, 2640–2657, doi:10.1002/2014JE004716.
743
744 Dehouck E., MCLennan, S. M., Skute, E. C., Dyar, M. D., 2017. Stability and fate of ferrihydrite during
745 episodes of water/rock interactions on early Mars: An experimental approach, J. Geophys. Res.,
746 10.1002/2016JE005222.

747 Fedo, C., Nesbitt H. W., Young, G.M., 1995. Unraveling the effects of potassium metasomatism in
748 sedimentary rocks and paleosols, with implications for paleoweathering conditions and provenance,
749 Geology, 23, 921–924.

750 Fedo C. et al., 2017. Facies Analysis And Basin Architecture Of The Upper Part Of The Murray Formation,
751 Gale Crater, Mars, 48th Lunar Planet. Sci. Conf., #1689.

752 Forni, O. et al., 2015. First detection of fluorine on Mars: implications for Gale crater's geochemistry,
753 Geophy. Res. Letters, doi:10.1002/2014GL062742.

754 Frydenvang J. et al., 2017. Diagenetic silica enrichment and late-stage groundwater activity in Gale crater,
755 Mars. Geophys. Res. Let., 44, 4716-4724.

756 Garzanti, E., Padoan, M., Andò, S., Resentini, A., Vezzoli, G., Lustrino, M., 2013. Weathering and relative
757 durability of detrital minerals in equatorial climate: sand petrology and geochemistry in the East African
758 Rift. The Journal of Geology 121, 547–580.

759 Grotzinger J. P., et al., 2014. A Habitable Fluvio-Lacustrine Environment at Yellowknife Bay, Gale Crater,
760 Mars, Science, 343, 10.1126/science.1242777.

761 Grotzinger, J. P., et al., 2015. Deposition, exhumation, and paleoclimate of an ancient lake deposit, Gale
762 crater, Mars, Science, 350, doi 10.1126/science.aac7575.

763 Hurowitz J. et al., 2017. Redox stratification of an ancient lake in Gale crater, Mars. Science, 356,
764 doi:10.1126/science.aah6849.

765 Lanza, N. L. et al., 2014. High manganese concentrations in rocks at Gale crater, Mars, Geophysical Res.
766 Letters, 41(16):5755-5763, doi:10.1002/2014GL060329.

767 Le Deit L., Hauber, E., Fueten, F., Pondrelli, M., Pio Rossi, A., Jaumann, R., 2013. Sequence of infilling events
768 in Gale Crater, Mars: Results from morphology, stratigraphy, and mineralogy, J. Geophys. Res., 118, 1-35.

769 Le Deit, L., et al., 2016. The potassic sedimentary rocks in Gale Crater, Mars, as seen by ChemCam on board
770 Curiosity, JGR-Planets, 121, 784-804.

771 Mangold, N. et al., 2015. Chemical variations in Yellowknife Bay formation sedimentary rocks analyzed by
772 ChemCam onboard the Curiosity rover on Mars, *JGR-Planets*, DOI: 10.1002/2014JE004681

773 Mangold N., et al., 2016. Composition of conglomerates analyzed by the Curiosity rover: Implications for
774 Gale crater crust and sediment sources, J. Geophys. Res.-Planets, 121, 353-387.

775 Mangold N. et al., 2017. Classification scheme for sedimentary and igneous rocks in Gale crater, Mars,
776 Icarus, 284, 1-17.

777 Maurice S., et al., 2012. The ChemCam Instrument Suite on the Mars Science Laboratory (MSL) Rover:
778 Science Objectives and Mast Unit Description, Space Sci Rev, 170:95–166, DOI 10.1007/s11214-012-9912-
779 2.

780 McLennan, S.M., 1993. Weathering and global denudation. The Journal of Geology 101, 295–303.

781 McLennan, S. M. et al., 2014. Elemental Geochemistry of Sedimentary Rocks in Yellowknife Bay, Gale
782 Crater, Mars. Science, 343, 10.1126/science.1244734.

783 Meslin, P.-Y., et al., 2013. Soil Diversity and Hydration as Observed by ChemCam at Gale Crater, Mars,
784 Science, 341, 0.1126/science.1238670.

785 Meunier A., Caner, L., Hubert, F., El Albani, A., Pret D., 2013. The Weathering Intensity Scale (Wis): An
786 Alternative Approach Of The Chemical Index Of Alteration (CIA). Am. J. Sci., 313, 113-143.

787 Milliken R., Grotzinger J. P., Thompson, B. J., 2010. Paleoclimate of Mars as captured by the stratigraphic
788 record in Gale crater. Geophy. Res. Let., 37, 2009GL041870.

789 Morris R. V. et al. (2016). Silicic volcanism on Mars evidenced by tridymite in high-SiO_2 sedimentary rock
790 at Gale crater, PNAS, 113, 7071-7076.

791 Morrison S. M., et al., 2018. Crystal chemistry of martian minerals from Bradbury Landing through Naukluft
792 Plateau, Gale crater, Mars, American Mineralogist, doi.org/10.2138/am-2018-6124.

793 Nachon, M., et al., 2014. Calcium sulfate veins characterized by the ChemCam instrument at Gale Crater,
794 Mars. J. Geophys. Res., 119, 1991-2016.

795 Nachon, M., et al., 2017 Chemistry of diagenetic features analyzed by ChemCam at Pahrump Hills, Gale
796 crater, Mars. Icarus, 281, 121-136. http://dx.doi.org/10.1016/j.icarus.2016.08.026 (2017).

797 Nesbitt, H. W., Young, G. M., 1982. Early Proterozoic climates and plate motions inferred from major
798 element chemistry of lutites, Nature, 299, p. 715–717.

799 Nesbitt, H.W., Young, G.M., 1996. Petrogenesis of sediment in the absence of chemical weathering: effects
800 of abrasion and sorting on bulk composition and mineralogy. Sedimentology 43, 341–358.

801 Newsom H. et al., 2017. Increasing Occurrence Of Sandstone Cemented With Calcium Sulfate On Mount
802 Sharp, Gale Crater, Mars. 48th Lunar Planet. Sci. Conf. #2495.

803 Ollila, A., et al., 2014. Trace Element Geochemistry (Li, Ba, Sr, and Rb) using Curiosity's ChemCam: Early
804 Results for Gale Crater from Bradbury Landing Site to Rocknest, J. Geophys. Res., 119, 18-31.

Parker, A, 1970. An index of weathering for silicate rocks, Geological Magazine, 107, 501-504.

Poulet, F., et al., 2009. Quantitative compositional analysis of Martian mafic regions using the MEx/OMEGA reflectance data: 2. Petrological implications, Icarus, 201, 84-101.

Rampe et al., 2017. Mineralogy of an ancient lacustrine mudstone succession from the Murray formation, Gale crater, Mars, Earth Planet. Sci. Let., 471, 172-185.

Rapin W., et al., 2016. Hydration state of calcium sulfates in Gale crater, Mars: identification of basanite veins, Earth Planet. Sci. Let., 452, 197-205.

Rivera-Hernandez, F. et al. 49th LPSC, abstract 2973, Houston, 2018.

Salvatore M.R., Mustard, J.F., Head, J.W., Cooper, R.F., Marchant, D.R., Wyatt, M.B., 2013. Development of alteration rinds by oxidative weathering processes in Beacon Valley, Antarctica, and implications for Mars, Geochemica Cosmochemica Acta, 115, 137-161.

Siebach, K. L., M. B. Baker, J. P. Grotzinger, S. M. McLennan, R. Gellert, L. Thompson, J. A. Hurowitz, 2017. Sorting out Compositional Trends in Sedimentary Rocks of the Bradbury Group (Aeolis Palus), Gale Crater, Mars, Journal of Geophysical Research, 122, 295-328.

Sheldon, N. D. Retallack, G. J., Tanaka, S., 2012. Geochemical Climofunctions from North American Soils and Application to Paleosols across the Eocene-Oligocene Boundary in Oregon, The Journal of Geology, 110, 687-696.

Stein, N., J.P. Grotzinger, J. Schieber, N. Mangold, B. Hallet, D.Y. Sumner, C. Fedo, 2018. Reply : Desiccation cracks provide evidence of lake drying on Mars, Sutton Island member, Murray formation, Gale Crater, Geology, 46, 515-518, doi.org/10.1130/G45237Y.1

Taylor S. R., McLennan, S. M., 2009. Planetary Crusts, Cambridge, 378pp.

Thorpe, M., Hurowitz, J., Dehouck, E., 2017. A Frigid Terrestrial Analog For The Paleoclimate Of Mars. Lunar Planet. Sci. Conf., 48th, #2599.

Treiman A. H., et al., 2016. Mineralogy, provenance, and diagenesis of a potassic basaltic sandstone on Mars: CheMin X-ray diffraction of the Windjana sample (Kimberley area, Gale Crater). J Geophys Res Planets, 121, 75–106.

Vaniman D. T., et al., 2014. Mineralogy of a mudstone at Yellowknife Bay, Gale crater, Mars. Science, 343.

Vaniman D. T., et al., 2017. Calcium Sulfates At Gale Crater And Limitations On Gypsum Stability 48th Lunar Planet. Sci. Conf., #1661.

Wiens, R. C., et al., 2012. The ChemCam Instrument Suite on the Mars Science Laboratory (MSL) Rover: Body Unit and Combined System Tests, Space Sci. Rev., doi 10.1007/s11214-012-9902-4.

839 Wilson M. J., 2004. Weathering of the primary rock-forming minerals: processes, products and rates. Clay
840 minerals, 39, 233-266.

841 Yang S., Ding, F., Ding, Z., 2006. Pleistocene chemical weathering history of Asian arid and semi-arid regions
842 recorded in loess deposits of China and Tajiki, Geochemica Cosmochemica Acta, 70 1695-1709.

843
844
845
846

847

848

849 **Tab 1:** Example of a single target with 10 observation points (Upper Hadlock, sol 1505). The target average
850 chemistry is obtained by removing point 5 which targeted a diagenetic feature (see Figure 2), and
851 averaging the remaining points. Note that the deviation around the average is relatively limited as
852 expected for homogeneous rocks with small grain size.

853

Upper Hadlock	SiO_2	TiO_2	Al_2O_3	FeO_T	MgO	CaO	Na_2O	K_2O	Sum
Point 1	56.4	1.03	12.50	17.0	4.60	2.70	2.52	0.93	97.79
Point 2	55.30	0.94	12.90	18.50	4.20	2.60	3.24	1.56	99.22
Point 3	57.20	0.99	11.80	15.80	4.20	2.30	2.73	1.66	96.71
Point 4	54.60	0.99	11.20	18.10	4.70	2.00	2.25	2.44	96.26
Point 5	*1.20*	*0.20*	*0.70*	*4.40*	*1.50*	*34.80*	*0.46*	*0.01*	*43.33*
Point 6	51.40	0.91	9.20	21.00	4.30	1.60	1.74	2.81	92.88
Point 7	53.30	0.91	10.00	20.60	4.00	1.70	1.85	2.74	95.08
Point 8	55.50	0.94	12.70	18.20	4.00	2.50	2.48	1.17	97.52
Point 9	55.80	0.98	12.50	17.20	4.30	2.50	2.84	1.17	97.22
Point 10	55.70	0.92	11.50	17.70	4.50	2.10	2.06	2.33	96.85
Average (without point 5)	**55.02**	**0.96**	**11.59**	**18.23**	**4.31**	**2.22**	**2.41**	**1.86**	**96.6**
Std Deviation	1.74	0.04	1.27	1.66	0.24	0.39	0.48	0.72	1.79

854

855

856

857

858 **Tab. 2:** CheMin quantitative mineralogy at Marimba used for mass balance calculation for estimating the
859 Fe^{2+}/Fe^{3+} ratio for the WIS calculation (from Bristow et al., 2018). The mineral abundances modeled and
860 presented here were updated compared to results currently available in the Planetary Data System.

861

862

Mineral	Whole rock (%)	FeO (wt%) in pure minerals	Fe_2O_3 (wt%) in pure minerals	FeO (wt%) contribution to sample	Fe_2O_3 (wt%) contribution to sample	Fe^{2+} (molar) in sample	Fe^{3+} (molar) in sample
Plagioclase	14.0	N/A	N/A				
Hematite	6.4	0	100	0	6.400	0	0.0401
Ca-sulfates	7.0	N/A	N/A	-	-	-	-
Sanidine	2.4	N/A	N/A	-	-	-	-
Pyroxene*	0.7	30.9	0	0.2163	0	0.00301	0
Jarosite**	0.7	0	47.83	0	0.335	0	0.0021
Quartz**	0.7	N/A	N/A	-	-	-	-
Amorphous	40	?	?	?	?	?	?
Clay minerals***	28	0	5.0	0	1.40	0	0.0088
Whole Rock iron content	99.9	N/A	N/A	0.2163	8.135	**0.00301**	**0.0509**

863

864 *Pyroxene composition assumed to be similar to the pigeonite from lower Murray drills (Morrison et al.,
865 2017).
866 **At detection limit. We use here a value of 0.7 wt.%, which is the typical lowest abundance quantifiable.
867 ***Clay minerals assumed with 5% Fe_2O_3 from CheMin diffractometer modeling (Bristow et al., 2018).
868

869 **Tab. 3** : Mineral abundances from CheMin data (Rampe et al., 2017, Bristow et al., 2018). Note that Mojave
870 and Telegraph Peaks compositions are strongly modified by diagenetic phases (jarosite, silica). Buckskin is
871 not included, given its presence in the high-silica region where ChemCam targets are excluded from the
872 present work.

873

Mineral	Confidence Hills (Pahrump Hills)	Mojave (Pahrump Hills)	Telegraph Peak (Pahrump Hills)	Oudam (Hartmann's Valley)	Marimba (Karasburg)	Quela (Karasburg)	Sebina (Sutton Island)
Plagioclase	20.4	23.5	27.1	27.8	14.0	13.5	10.7
Sanidine	5.0	-	5.2	-	2.4	2.3	1.4
Olivine	1.2	0.2	1.1	-	-	-	-
Pyroxenes	13.8	7.0	7.6	5.3	0.7	2.7	2.8
Quartz	0.7	0.8	0.9	0.7	At detection limite	At detection limit	At detection limit
Hematite	6.8	3.0	1.1	13.9	6.4	7.1	6.9
Magnetite	3.0	3.0	8.2	-	-	-	-
Ca-sulfates	-	-	-	6.3	7.0	5.5	7.4
Apatite	1.3	1.8	1.9	-	-	-	-
Jarosite	1.1	3.1	1.5	-	At detection limit	At detection limit	0.9
Silica	-	-	18.2	-	-	-	-
Clay minerals	7.6	4.7	-	3	28	16	19
Amorphous	39.2	53	27.2	43	40	52	51.1

874

875

876

877 Table 4: Summary of various CIA values found on Mars with Earth as comparison.

878

Rock type	Value	Reference
Fresh basaltic rock, Earth	35-40	Babechuk et al., 2014
Fresh continental crust, Earth	45-50	Nesbitt and Young, 1996
Average Mars crust	37	McLennan et al., 2014
Bradbury formation, Sheepbed member, Mars	35-40	McLennan et al., 2014
Bradbury formation conglomerates, Mars	44	This study
Bradbury formation, Kimberley, Mars	30-40	This study
Murray formation, Pahrump Hills member, Mars	~50	Hurowitz et al., 2017
Murray formation, Sutton island member, Mars	48-63	This study

879